






**Please cite the Published Version**

Fang, Kai , Tong, Lianghuai, Xu, Xiaojie, Cai, Jijing , Peng, Xueyuan, Omar, Marwan , Bashir, Ali Kashif  and Wang, Wei  (2025) Robust Fault Diagnosis of Drilling Machinery Under Complex Working Conditions Based on Carbon Intelligent Industrial Internet of Things. IEEE Internet of Things Journal. ISSN 2372-2541

**DOI:** <https://doi.org/10.1109/jiot.2025.3542404>

**Publisher:** Institute of Electrical and Electronics Engineers (IEEE)

**Version:** Accepted Version

**Downloaded from:** <https://e-space.mmu.ac.uk/638636/>

**Usage rights:**  In Copyright

**Additional Information:** This is an accepted manuscript of an article which appeared in IEEE Internet of Things Journal

**Enquiries:**

If you have questions about this document, contact [openresearch@mmu.ac.uk](mailto:openresearch@mmu.ac.uk). Please include the URL of the record in e-space. If you believe that your, or a third party's rights have been compromised through this document please see our Take Down policy (available from <https://www.mmu.ac.uk/library/using-the-library/policies-and-guidelines>)

# Robust Fault Diagnosis of Drilling Machinery under Complex Working Conditions Based on Carbon Intelligent Industrial Internet of Things

Kai Fang, Lianghuai Tong, Xiaojie Xu, Jijing Cai, Xueyuan Peng, Marwan Omar, Ali Kashif Bashir, and Wei Wang

**Abstract**—As sustainable development gains attention, integrating carbon-intelligent computing into fault diagnosis systems has emerged as a critical strategy to reduce energy consumption and carbon footprints. This approach uses Artificial Intelligence (AI) and the Internet of Things (IoT) to optimize task scheduling, aligning it with low-carbon energy sources based on time and location. In fault diagnosis, energy-intensive tasks such as data processing and model inference can be scheduled during periods of abundant renewable energy, thereby minimizing emissions. However, drilling machines operate under complex conditions that generate non-stationary noise, which distorts signals and complicates fault diagnosis. Therefore, this paper combines Bidirectional Long Short-Term Memory (BiLSTM) with the Kolmogorov-Arnold Network (KAN) and integrates Wavelet Transform and Convolutional Autoencoder, proposing a highly robust fault diagnosis model for drilling machines, named WCBK. The Wavelet Transform converts pressure time-series data, which contains fault information, into time-frequency images, facilitating the detection of fault frequency components. The Convolutional Autoencoder preserves essential features while removing noise by learning low-dimensional representations of the signal, effectively capturing local features in time-frequency images through local connections to enhance denoising performance. Finally, the composite deep learning network, which combines BiLSTM and KAN, achieves highly robust fault diagnosis under complex working conditions. The effectiveness

of the proposed WCBK model was validated through ablation experiments, experiments on different individuals, experiments on different parts, and model adaptability evaluations. In experiments involving different individuals and parts, the WCBK model improved fault diagnosis accuracy by 10.9% and 8.8%, respectively, compared to existing models.

**Index Terms**—Carbon-intelligent Computing, IoT, Fault Diagnosis, Noise Filtering, BiLSTM, KAN.

## I. INTRODUCTION

As a critical piece of equipment in modern industry and infrastructure construction, drilling machines play a vital role in resource extraction, geological exploration, and infrastructure development. With the increasing emphasis on sustainability [1], [2], [3], the interaction of carbon-intelligent computing into the operation and fault diagnosis of drilling machines has gained significant attention. Carbon-intelligent computing optimizes energy consumption by scheduling high-energy tasks, such as data processing and fault prediction, with periods of low-carbon energy availability. This approach not only reduces the carbon footprint of drilling operations but also enhances operational efficiency. By incorporating technological innovations and equipment upgrades alongside carbon-intelligent solutions, construction efficiency can be improved, economic benefits maximized, and production safety significantly enhanced, making these strategies both strategically important and practically valuable. Drilling machines are designed to penetrate thick and hard rock layers to achieve specific operational targets, requiring sustained high-load operation. However, this operational demand imposes substantial stress on mechanical components, accelerating metal fatigue and promoting the formation of cracks. Over time, the progressive accumulation of such damage can lead to the failure or breakage of critical mechanical parts. Therefore, the implementation of timely and effective fault diagnosis is essential for prolonging equipment lifespan, ensuring operational safety, and reducing downtime.

While fault diagnosis is crucial for drilling machines, it faces significant challenges in practical applications. The complex operating conditions of drilling machinery, influenced by factors such as rock properties, workload, and temperature, generate significant vibration, impact, and environmental noise. These interferences often distort sensor signals, complicating the fault diagnosis process. Noise components in the signals can obscure genuine fault characteristics, making

This work was supported by the State Administration for Market Regulation of Science and Technology Project under grant no. 2023MK050; National Natural Science Foundation of China under grant no.62403433; Zhejiang Provincial Natural Science Foundation of China under grant no. LQ23F020-001; Quzhou City Science and Technology Project under grant no. 2023K252, 2023K248, and 2023NC08.

Kai Fang is with the College of Energy and Power Engineering, Xi'an Jiaotong University, Xi'an 710049, China; Quzhou Academy of Metrology and Quality Inspection, Quzhou 324000, China. (Email: kaifang@xjtu.edu.cn)

Lianghuai Tong and Xiaojie Xu are with the Quzhou Academy of Metrology and Quality Inspection, Quzhou 324000, China. (Email: cscpcv@163.com and 38767676@qq.com)

Jijing Cai is with the College of Mathematics and Computer Science, Zhejiang A&F University, Hangzhou 311300, China. (Email: Jijing-cai19@gmail.com)

Xueyuan Peng is with the College of Energy and Power Engineering, Xi'an Jiaotong University, Xi'an 710049, China. (Email: xypeng@mail.xjtu.edu.cn)

Marwan Omar is with the Information Technology and Management, Illinois Institute of Technology, USA. (Email: momar3@iit.edu)

Ali Kashif Bashir is with the Department of Computing and Mathematics, Manchester Metropolitan University, UK; Centre for Research Impact & Outcome, Chitkara University Institute of Engineering and Technology, Chitkara University, Rajpura, 140401, Punjab, India. (Email: dr.alikashif.b@ieee.org)

Wei Wang is with the Guangdong-Hong Kong-Macao Joint Laboratory for Emotion Intelligence and Pervasive Computing, Artificial Intelligence Research Institute, Shenzhen MSU-BIT University, Shenzhen 518172, China, and are also with the School of Medical Technology, Beijing Institute of Technology, Beijing 100081, China. (Email: ehome.wang@gmail.com).

Corresponding author: Xueyuan Peng

fault detection more difficult. Complex noise may cause the fault diagnosis system to mistakenly identify noise signals as faults, increasing the false alarm rate. This not only wastes maintenance resources but also causes unnecessary downtime and disrupts production schedules. Additionally, noise interference can obscure actual fault signals, increasing the risk of missed detections. Such oversights prevent the system from identifying and addressing issues promptly, potentially leading to further equipment damage and compromising operational safety.

The development of modern technology has provided innovative solutions for fault diagnosis in drilling machinery. By introducing sensor technology [4], [5], the Internet of Things [6], [7], [8], and advanced deep learning algorithms [9], [10], [11], it is possible to monitor the operational status of drilling machinery in real-time and detect faults promptly [12]. Traditional fault diagnosis methods, which rely heavily on expert knowledge and manual feature extraction, are being supplanted by deep learning approaches capable of automatically learning and extracting features. This shift has significantly improved the accuracy and efficiency of fault diagnosis. Deep learning models such as Convolutional Neural Networks (CNN) [13] and Recurrent Neural Networks (RNN) are particularly adept at handling complex nonlinear data and identifying subtle fault characteristics in rotating machinery. Tang A et al. [14], from a data-driven perspective, proposed a fault diagnosis method for the fluid end of drilling pumps based on Generalized S-transform (GST) and CNN. Vibration signals from the fluid end were analyzed, with GST converting these signals into time-frequency images to enhance the characterization of fault features. The study addressed challenges related to noise pollution in vibration signals, which often obscure feature information and hinder extraction. By introducing batch normalization and optimizing the number of neurons in the fully connected layers, the AlexNet model was refined to classify the fluid end's operational states, including normal, slightly damaged, and severely damaged conditions. Chen et al. [15] proposed a novel Multi-Scale Shared Learning Network (MSSLN) architecture to extract and classify the inherent fault features of vibration signals at multiple scales. This architecture combines hierarchical activation with multi-scale stream fusion, enabling the network to fully capture consistent shared representations among multi-scale factors. This characteristic helps MSSLN provide more reliable diagnostics than existing single-scale and multi-scale methods. Song et al. [16] introduced a fault detection method combining Fault-Targeted Gated Recurrent Units (FTGRU) and Canonical Correlation Analysis (CCA). FTGRU was employed to extract temporal features sensitive to early-stage faults, improving detection accuracy. CCA was subsequently applied to construct the fault detection model. To enhance robustness, a multi-layer strategy was proposed: the first layer employed a basic CCA model, while the second layer activated the FTGRU-CCA method if no faults were detected in the initial layer. The method was validated through two industrial case studies.

To enhance fault diagnosis capabilities for drilling machines under complex working conditions, this paper proposes a highly robust fault diagnosis model, WCBK. Firstly, the

Wavelet Transform is applied to convert pressure time-series data into time-frequency images, providing information in both the time and frequency domains. This approach effectively captures the frequency variations of the signal at different time points and provides a robust solution for handling substantial amounts of complex non-stationary noise. Next, a Convolutional Autoencoder is used to extract the features of the input images. Through the joint training of the encoder and decoder structure, the Convolutional Autoencoder can learn a compressed representation of the input images and reconstruct clear images, thereby removing noise. Finally, the model integrates BiLSTM and KAN. The bidirectional structure of BiLSTM captures dependencies in both forward and backward sequences, improving the representation of fault features. In contrast, KAN abandons the linear weight matrix and utilizes a combination of continuous functions to represent high-dimensional data. This approach enhances its ability to handle key fault features, thereby improving the accuracy of fault diagnosis. Here are the main contributions of this paper:

- Complex working conditions generate a substantial amount of non-stationary noise, composed of multiple frequency components, which is challenging to eliminate using a single frequency filter. To address this issue, this paper first applies Wavelet Transform to convert time-series data into time-frequency images, thereby facilitating the preliminary separation of signals from different frequency bands. Subsequently, a Convolutional Autoencoder further processes the time-frequency images, learning low-dimensional representations and performing feature reconstruction, thereby effectively mitigating complex multi-frequency noise.
- In long sequence fault data, fault features often represent a small fraction of the overall dataset, while normal state features tend to dominate, making it challenging to identify and extract the fault features. A single neural network architecture is insufficient for efficient feature extraction and fault diagnosis in such complex data. To address this challenge, this paper proposes a composite neural network model, BiLSTM-KAN, for efficient fault feature extraction. The BiLSTM model captures temporal dependencies within fault features, improving detection of dynamic fault patterns. The KAN model replaces traditional weight matrices with continuous functions to better handle complex fault features. The combination of BiLSTM and KAN enhances the model's ability to process nonlinear fault patterns and improves fault diagnosis accuracy.
- This paper evaluates the effectiveness of the model through the implementation of ablation experiments, individual experiments, positional experiments, and model adaptation experiments. The results of these experiments demonstrate that the WCBK model exhibits an improvement in fault diagnosis accuracy of 10.9% and 8.8%, respectively, compared to the existing model.

The remainder of this paper is organized as follows: Section II presents related work, Section III discusses noise interference analysis, Section IV describes the model methodology,

Section V presents the experiments, and Section VI concludes the paper.

## II. RELATED WORK

### A. Noise filtering

Noise filtering is crucial in the fault diagnosis process of drilling machinery. It enhances signal quality and diagnostic accuracy, reduces false alarms and missed detections, optimizes maintenance strategies, and ensures safe operation. Yin et al. [17] introduced a tap-segmented Volterra filter, where an extensive-tap Volterra filter is decomposed into several short-tap filters using the closest Kronecker decomposition. Since the decomposed filters have significantly fewer taps than the original filter, the suggested approach substantially lowers the implementation expenses of the Volterra filter. Zhu et al. [18] introduced the random Fourier filter-based filtered-x least mean square algorithm, a random Fourier filter to handle impulse noise, simplifying computation through a cascaded model. Zheng et al. [19] proposed the Type I Filter, a low-complexity noise suppression filter that outperformed current methods, such as the Moving Average Algorithm, under severe noise conditions. Lone et al. [20] suggested a nearest-neighbor filtering method to reduce impulse noise by leveraging pixel correlation. Wang et al. [21] developed multi-channel noise reduction filters in the short-time-Fourier-transform domain, showing their iterative filter's advantages over traditional filters. Brahmi et al. [22] combined adaptive median, 2D adaptive Wiener, and adaptive local noise reduction filters for seismic data, improving fault structure imaging. Qiao et al. [23] proposed an improved Kalman filtering algorithm with adaptive sliding windows and variational Bayesian techniques for better noise robustness. Liu et al. [24] introduced a Maximum Entropy Kalman fusion filter, achieving better estimation performance under non-Gaussian noise. Lee et al. [25] developed a backward error analysis framework for adaptive recursive least squares filters, which facilitates the use of lower-precision arithmetic in adaptive filtering.

### B. Fault diagnosis

Fault diagnosis in mechanical operations ensures safe operation, extends equipment lifespan, reduces maintenance costs, improves production efficiency, and enhances product quality, making it crucial in modern industry. Zhang et al. [26] proposed a Selective Kernel Convolutional Deep Residual Network, which integrates channel-spatial attention mechanisms and feature fusion for mechanical fault diagnosis. This model effectively extracts fault features from vibration signals, improving diagnosis efficiency. Yu et al. [27] introduced a fault diagnosis framework based on Graph Neural Networks (GNN) and Dynamic Graph Embedding. CNN extracts hidden fault features from raw signals, and GNN further identifies fault features sensitive to operating condition fluctuations. A "node electorate" mechanism optimizes fault pattern recognition. Yan et al. [28] presented an automatic fault detection and diagnosis method using Transformer Conditional Wasserstein Generative Adversarial Network coupled with Deep Reinforcement

Learning. This method synthesizes and selects high-quality fault data samples, which are then integrated with real fault samples to train traditional classifiers. Xue et al. [29] proposed a motor-bearing fault diagnosis framework that leverages multi-transform domain analysis and multi-source data fusion. This approach enables the extraction of features from the time, frequency, and time-frequency domains. Zhao et al. [30] developed an adaptive decomposition algorithm based on Improve Complete Ensemble Empirical Mode Decomposition with Adaptive Noise and fractal dimension analysis. Combined with CNN, this method offers intelligent fault diagnosis by employing principal component analysis and fractal dimension to select and reconstruct sub-signals for feature extraction and pattern recognition. Qiang et al. [31] introduced a real-time fault diagnosis method based on transmission control unit signal time series feature pattern recognition. By establishing time series patterns from different fault sources, the method applies variational mode decomposition and signal selection for feature extraction.

## III. ANALYSIS OF NOISE INTERFERENCE WITH THE ORIGINAL SIGNAL

This paper employs a simulation approach to investigate the interference affecting drilling machinery under complex working conditions. The simulation employs composite noise, which consists of Gaussian noise and uniform noise. Gaussian noise is used to simulate random environmental interference and unpredictable fluctuations within the equipment, whereas uniform noise is employed to represent systematic and evenly distributed external interference, such as equipment vibrations and mechanical resonance. The combined effect of these noise types on the pressure time series data  $X(t)$  of the drilling machine is represented as a superposition, which more accurately reflects the complex interference factors present in real-world working environments. The generation of a simulated dataset encompassing various interference factors is achieved by overlaying composite noise onto the original pressure time series data. The enhanced dataset offers a more profound comprehension of the influence of noise on drilling machine pressure signals, thereby establishing a basis for subsequent fault diagnosis in the context of interference. In this paper,  $I_G(t)$  represents the Gaussian noise,  $I_E(t)$  represents the uniform noise, and the composite noise is denoted as  $I_N(t) = I_G(t) + I_E(t)$ . The pressure time series data after applying noise interference is represented as:

$$X_{noise}(t) = X(t) + I_N(t) \quad (1)$$

### A. Gaussian noise

In this paper, Gaussian noise  $I_G(t)$  is used to simulate random environmental interference and unpredictable fluctuations within the equipment [32], [33]. The mathematical representation of Gaussian noise is derived from the normal distribution, which provides a probabilistic description of its characteristics. The probability density function of Gaussian noise  $I_G$  is expressed as:

$$p_G(x) = \frac{1}{\eta\sqrt{2\pi}} \exp\left(\frac{-(x - \mu)^2}{2\eta^2}\right) \quad (2)$$

where  $\mu$  represents the mean value of the noise,  $\eta$  represents the range of noise fluctuations, and  $\eta^2$  represents the degree of noise dispersion. The Gaussian noise  $I_G(t)$  at time  $t$  can be represented as a random variable that follows the above normal distribution. For Gaussian noise with a mean value of  $\mu$  and a standard deviation of  $\eta$ , it can be expressed as:

$$I_G(t) = \mu + \eta \cdot Z(t) \quad (3)$$

where  $Z(t)$  is a standard normal distribution random variable.

### B. Uniform noise

The article models systematic and uniformly distributed external disturbances, such as equipment vibrations and mechanical resonances, using balanced noise  $I_E(t)$ . Balanced noise is a type of noise with uniform distribution characteristics, where its probability density function is constant within a defined interval. The specific expression of balanced noise can be represented using a uniform distribution. For balanced noise over an interval  $[a, b]$ , its probability density function is expressed as follows:

$$p_E(x) = \begin{cases} \frac{1}{b-a} & a \leq x \leq b \\ 0 & otherwise \end{cases} \quad (4)$$

The balanced noise  $I_E(t)$  at time  $t$  can be represented as a random variable following a uniform distribution  $U(a, b)$ . The process is expressed as:

$$I_E(t) \sim U(a, b) \quad (5)$$

Generate a standard uniformly distributed random number  $U(t)$  within the interval  $[0, 1]$ . Convert this uniformly distributed random number to the target interval  $[a, b]$  to obtain the balanced noise  $I_E(t)$ . The related process is expressed as follows:

$$I_E(t) = a + (b - a) \cdot U(t) \quad (6)$$

### C. Variation of pressure signal under noise interference

Fig. 1 provides a visual representation of how pressure signals are affected by varying levels of noise interference. Fig. 1(a) compares the original pressure signal with the signal impacted by composite noise at an intensity of 0.3, while Fig. 1(b) illustrates the effect of composite noise at an intensity of 0.7.

Fig. 1(a) depicts a relatively low noise intensity, wherein the noise-interfered signal exhibits a waveform that is largely consistent with the original signal, exhibiting comparable trends, peaks, and valleys. The distortion of the signal due to noise is not significant; rather, the interference mainly manifests as an increase in local minor fluctuations. As the noise intensity rises in Fig. 1(b), the discrepancies between the interfered signal and the original signal become more pronounced. While the general trend can still be discerned, the accuracy and reliability of the data are significantly compromised. The interference affects all areas with greater prominence, particularly in the high and low peak regions, resulting in considerable data deviations and impairing the accuracy of fault diagnosis.

In conclusion, an increase in noise intensity markedly affects the accuracy and usability of the pressure signal for

fault diagnosis. Consequently, denoising and signal recovery are essential steps to ensure the accuracy of fault diagnosis.

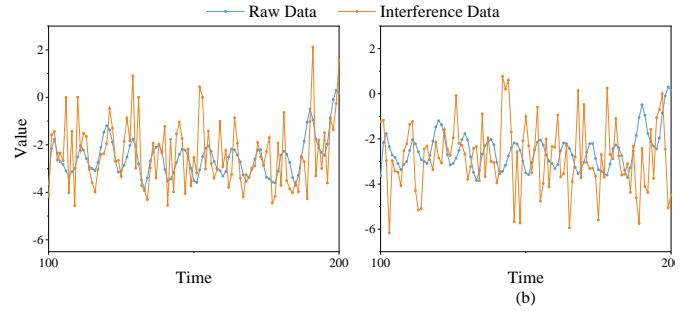


Fig. 1. Variation of raw pressure signal under different intensity of noise interference. (a) Comparison of signal curves at noise intensity 0.3. (b) Comparison of signal curves at noise intensity 0.7.

## IV. METHODOLOGIES

The proposed high-robustness fault diagnosis model for drilling machinery under complex working conditions, designated WCBK, is depicted in Fig. 2. The model can be divided into three principal sections. The initial phase of the process entails the creation of a fault dataset for the drilling machine in the presence of composite noise interference. In this phase, the pressure time series data of the drilling machine under various faults are gathered, and a composite noise comprising Gaussian noise and uniform noise is employed to emulate the interference encountered by the drilling machine in complex operational conditions. The outcome is a dataset containing fault data with noise interference, which serves as the foundation for subsequent diagnostic processes. The second phase is the noise-filtering process. This phase comprises a Wavelet Transform and Convolutional Autoencoder. Initially, the Wavelet Transform is employed to transform the time series into time-frequency images, thereby decomposing the signal into distinct frequency bands to achieve preliminary noise filtering. Subsequently, a Convolutional Autoencoder is employed for additional denoising. The Convolutional Autoencoder effectively preserves essential signal features while removing extraneous noise by learning a compressed representation in low-dimensional space. Furthermore, local connections and weight-sharing mechanisms are employed to more effectively capture local features in the time-frequency images, thereby enhancing the denoising effect. The inverse Wavelet Transform is then applied to transform the time-frequency images back into the time series. The third phase is the composite neural network, which is comprised of the BILSTM and KAN models. The bidirectional structure of the BILSTM model enables it to capture the feature information of forward and backward dependencies in the sequence, thereby enhancing the expression of fault features. In contrast to the linear weight matrix, the KAN model employs a combination of continuous functions to express high-dimensional functions, thus enhancing its ability to handle critical fault features and improving the accuracy of fault diagnosis.

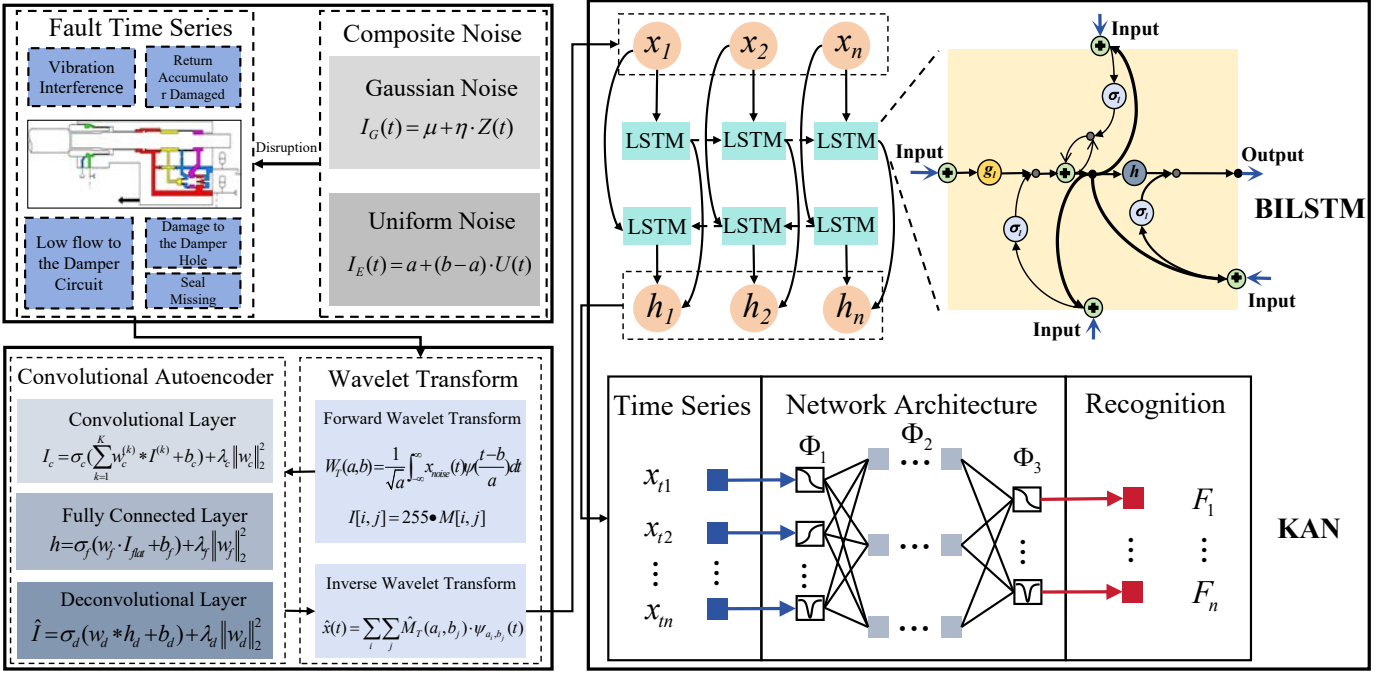


Fig. 2. Flowchart of the overall framework of the WCBK model

### A. Wavelet transform

Wavelet Transform [34], [35] on pressure time series under interference involves selecting wavelet mother function  $\psi(t)$  and scale  $a$ . The Wavelet Transform of the time series data  $X_{noise}(t)$  is defined as:

$$W_T(a, b) = \frac{1}{\sqrt{a}} \int_{-\infty}^{\infty} X_{noise}(t) \psi\left(\frac{t-b}{a}\right) dt \quad (7)$$

where  $a$  controls the stretching of the wavelet function, while the position parameter  $b$  determines its placement in time. Equation (7) measures how similar the input signal  $X_{noise}(t)$  is to the wavelet functions at different scales and positions. For each combination of  $a$  and  $b$ , a wavelet coefficient  $W_T(a, b)$  is calculated, indicating the energy of the signal at that particular scale and time.

Subsequently, the calculated wavelet coefficients are systematically arranged into a two-dimensional matrix  $M$ , where the element  $M_{i,j}$  corresponds to the wavelet coefficients at specific scales  $a_i$  and time positions  $b_j$ . This process is expressed as:

$$M_T = \begin{bmatrix} W_T(a_1, b_1) & W_T(a_1, b_2) & \cdots & W_T(a_1, b_n) \\ W_T(a_2, b_1) & W_T(a_2, b_2) & \cdots & W_T(a_2, b_n) \\ \vdots & \vdots & \ddots & \vdots \\ W_T(a_m, b_1) & W_T(a_m, b_2) & \cdots & W_T(a_m, b_n) \end{bmatrix} \quad (8)$$

where  $M_T$  represents the features of the signal  $X_{noise}(t)$  across different scales and time points, allowing for effective analysis and visualization of its time-frequency characteristics.

This structure also facilitates subsequent signal processing tasks, such as signal reconstruction and feature extraction. Since wavelet coefficients can exhibit significant variability,

normalization ensures that the coefficients are accurately represented when converted into an image format. The normalization process is expressed as follows:

$$M_{Tnorm}[i, j] = \frac{M_T[i, j] - \min(M_T)}{\max(M_T) - \min(M_T)} \quad (9)$$

where  $M_T[i, j]$  represents an element within the original wavelet coefficient matrix, while  $\min(M_T)$  and  $\max(M_T)$  signify the minimum and maximum values, respectively, within the coefficient matrix  $M_T$ .

Subsequently, the normalized coefficient matrix  $M_{Tnorm}[i, j]$  is mapped to a time-frequency image. The aforementioned process is expressed as follows:

$$I[i, j] = 255 \cdot M_{Tnorm}[i, j] \quad (10)$$

where  $I[i, j]$  represents the grayscale value of the corresponding pixel in the time-frequency image, ranging from 0 (completely black) to 255 (completely white). This ensures that the dynamic range of the wavelet coefficients is fully expressed in the grayscale levels of the time-frequency image. Each element in  $I[i, j]$  corresponds to a pixel in the time-frequency image  $I$ , so matrix  $I[i, j]$  can be equivalently represented as the time-frequency image  $I$ .

### B. Convolutional autoencoder

The time-frequency image  $I$  undergoes denoising through a Convolutional Autoencoder[36], [37], as depicted in Fig. 3. This process involves sequential convolutional, pooling, fully connected, and deconvolutional operations. In the convolution layer Conv, the processing of the time-frequency image  $I$  is as follows:

$$I_{fconv} = \sigma\left(\sum_{k=1}^K w_c^{(k)} \cdot I^{(k)} + b_c\right) + \lambda_c \|w_c\|_2^2 \quad (11)$$



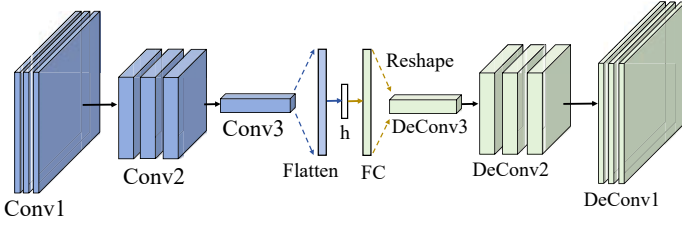


Fig. 3. Convolutional autoencoder specific structure schematic diagram

where  $I_{fconv}$  represents the feature map of the time-frequency image  $I$ , obtained after processing through the convolutional layer.  $\sigma_c$  represents the activation function of the convolutional layer,  $w_c^{(k)}$  denotes the weight of the  $k$ -th filter in the layer,  $b$  signifies the bias term of the layer,  $\lambda_c$  represents the regularization parameter of the layer, and  $\|w_c\|_2^2$  indicates the L2 norm of  $w_c$ . The feature map  $I_{fconv}$  is subsequently subjected to a Flatten operation, resulting in a one-dimensional array  $I_{flat}$ , which is then input into the fully connected layer.

The Flatten operation linearizes the spatial and channel information from the convolutional layer, allowing the data to be weighted and summed by the weights and biases of each neuron in the fully connected layer. This process is expressed as:

$$\begin{aligned} I_{flat} &= \text{flatten}(I_{fconv}) \\ h &= \sigma_{fc}(w_{fc} \cdot I_{flat} + b_{fc}) + \lambda_{fc} \|w_{fc}\|_2^2 \end{aligned} \quad (12)$$

where  $h$  represents the one-dimensional array obtained after the weighted sum in the fully connected layer.  $\sigma_{fc}$ ,  $w_{fc}$ ,  $b_{fc}$ , and  $\lambda_{fc}$  refer to the activation function, weight matrix, bias term, and regularization parameter of the fully connected layer, respectively, with  $\|w_{fc}\|_2^2$  representing the L2 norm of  $w_{fc}$ .

Subsequently, the one-dimensional array  $h$  undergoes a Reshape operation, which adjusts the output of the fully connected layer back to the dimensions and shape acceptable by the deconvolution layer. This process is expressed as:

$$\begin{aligned} h_{reshape} &= \text{reshape}(h) \\ \hat{I} &= \sigma_{de}(w_{de} \cdot h_{reshape} + b_{de}) + \lambda_{de} \|w_{de}\|_2^2 \end{aligned} \quad (13)$$

where  $\sigma_{de}$ ,  $w_{de}$ ,  $b_{de}$ , and  $\lambda_{de}$  are the activation function, weight matrix, bias term, and regularization parameter of deconvolution layer, respectively, and  $\|w_{de}\|_2^2$  is the L2 norm of  $w_{de}$ .

The denoised time-frequency image,  $\hat{I}$ , is converted back into a time series through inverse Wavelet Transform. By remapping the time-frequency image data back into the form of wavelet coefficients, the process is as follows:

$$\hat{M}_T[i, j] = \hat{I}[i, j] \cdot (\max(M_T) - \min(M_T)) + \min(M_T) \quad (14)$$

where  $\hat{I}[i, j]$  represents the normalized coefficient value extracted from the time-frequency image  $\hat{I}$ , which is generated by the autoencoder.  $M_T$  denotes the original wavelet coefficient matrix, while  $\hat{M}_T[i, j]$  signifies the result of converting these values back to the original wavelet coefficient scale.

Subsequently, the recovered wavelet coefficients, designated as  $\hat{M}_T$ , are converted back to time series data through the application of the inverse Wavelet Transform. This entails

employing the identical wavelet mother function utilized in the forward Wavelet Transform, albeit with the operation reversed. This process is expressed as follows:

$$\hat{x}(t) = \sum_i \sum_j \hat{M}_T(a_i, b_j) \cdot \psi_{a_i, b_j}(t) \quad (15)$$

where  $\hat{x}(t)$  represents the reconstructed time series data of the faults observed in the drilling machine,  $\hat{M}_T(a_i, b_j)$  denotes the recovered wavelet coefficients, and  $\psi_{a_i, b_j}(t)$  signifies the wavelet basis function adjusted for the corresponding scale and translation.

### C. BILSTM-KAN

The reconstructed fault signal,  $\hat{x}(t)$ , obtained through Wavelet Transform, Convolutional Autoencoder processing, and inverse Wavelet Transform, is then fed into the composite neural network BILSTM-KAN for fault diagnosis. The BILSTM neural network model is composed of bidirectional LSTM [38]. The forget gate in the LSTM determines how much of the past information should be forgotten at the current time step. The equation for the forget gate can be expressed as:

$$f_t = \sigma(W_f \cdot [h_{t-1}, \hat{x}_t] + b_f) \quad (16)$$

where  $\sigma$  represents the sigmoid activation function, which is employed to scale the input values to the range  $[0, 1]$ .  $h_{t-1}$  signifies the hidden state derived from the preceding time step, while  $W_f$  denotes the forget gate's weight matrix, which is applied to the previous hidden state and the current input.  $b_f$  represents the forget gate's bias term, and  $f_t$  signifies the forget gate's output.

The input gate in the LSTM network determines the quantity of novel information that should be incorporated into the memory cell at the present time step. The equation that relates to the input gate is expressed as follows:

$$i_t = \sigma(W_i \cdot [h_{t-1}, \hat{x}_t] + b_i) \quad (17)$$

where  $W_i$  and  $b_i$  represent the weight matrix and bias term of the input gate, respectively, and  $i_t$  denotes the output of the input gate.

Furthermore, the new candidate memory cell information  $\tilde{c}_t$  is generated using the tanh function, thereby ensuring that the values remain within the specified range of  $[-1, 1]$ . The related equation is expressed as follows:

$$\tilde{c}_t = \tanh(W_c [h_{t-1}, \hat{x}_t] + b_c) \quad (18)$$

where  $W_c$  and  $b_c$  represent the weight matrix and bias term of the candidate memory cell, respectively.

The process of updating the memory cell with the candidate memory cell information  $\tilde{c}_t$  is described as follows:

$$c_t = f_t \cdot c_{t-1} + i_t \cdot \tilde{c}_t \quad (19)$$

where  $c_{t-1}$  represents the cell state of the previous time step.

The output gate in the LSTM network is responsible for determining the output information at the current time step. The related equation is expressed as follows:

$$o_t = \sigma(W_o [h_{t-1}, \hat{x}_t] + b_o) \quad (20)$$

where  $W_o$  and  $b_o$  represent the weight matrix and bias term of the output gate, respectively.

The final hidden state information is scaled by applying the tanh function to the state of the memory cell. The related equation is expressed as follows:

$$h_t = o_t \cdot \tanh(c_t) \quad (21)$$

The forward and backward hidden states,  $\vec{h}_t$  and  $\overleftarrow{h}_t$ , respectively, are computed from the drilling machine fault time series data,  $\hat{x}(t)$ . The final hidden state,  $H_t = [\vec{h}_t, \overleftarrow{h}_t]$ , is produced by the BiLSTM. These hidden states contain the features of the drilling machine fault time series,  $\hat{x}(t)$ , which are then input into the KAN network for further processing and fault diagnosis.

The KAN model is developed based on the Kolmogorov-Arnold representation theorem [39]. The fundamental concept of KAN is to decompose high-dimensional functions into a series of one-dimensional functions, thereby enhancing the model's capacity for expression and interpretability. In KAN, weight parameters are replaced with univariate functions, typically represented by B-splines. In this context, the univariate function is represented by  $\phi_{j,i}$ , where  $j$  and  $i$  denote the output and input indices, respectively. For each layer input  $x_i$ , the output  $y_j$  is calculated. This process is expressed as follows:

$$y_j = \sum_{i=1}^d \phi_{j,i}(x_i) \quad (22)$$

The deep structure of KAN is achieved through the stacking of multiple layers of univariate functions. The output of each layer is utilized as the input for the subsequent layer. If there are  $L$  layers, the computation for each layer can be expressed as follows:

$$y_j^{(l+1)} = \sum_{i=1}^{n_l} \phi_{j,i}^{(l)}(y_i^{(l)}) \quad (23)$$

where  $y_j^{(l+1)}$  represents the output of the  $(l+1)$ -th layer,  $y_i^{(l)}$  signifies the output of the  $l$ -th layer,  $n_l$  denotes the number of nodes in the  $l$ -th layer, and  $\phi_{j,i}^{(l)}$  represents the univariate function of the  $l$ -th layer. The final output of the KAN is determined by the result of the last layer's computation. The related process is expressed as follows:

$$y_{output} = (\Phi_{l-1} \circ \Phi_{l-2} \circ \dots \circ \Phi_1 \circ \Phi_0)(H_t) \quad (24)$$

where  $\Phi$  is the spline function matrix, and  $y_{output}$  represents the result of the fault diagnosis.

## V. EXPERIMENT

### A. Dataset and experimental configuration

The dataset utilized in this study was derived from the 2022 PHM competition [40]. The data were procured from hydraulic drilling machinery, with faults introduced during the data collection process. Hydraulic pressure was monitored at a frequency of 50 kHz at three distinct locations, yielding comprehensive pressure time-series data for each fault. The schematic diagram of the test setup is illustrated in Fig. 4 [40], the different acquisition positions are shown in Table I, and the 10 fault types and their corresponding labels are shown in Table II.

TABLE I  
DESCRIPTION OF DIFFERENT COLLECTION POSITIONS

Position	Description
pdmp	Pressure at the inlet fitting during percussion
pin	Pressure within the outer chamber of the damper
po	Pressure in the volume behind the piston

TABLE II  
FAULT LABELS AND FAULT DESCRIPTIONS

Label	Description
NF	Normal
T	Increased thickness of drill pipe
A	A-seal missing
B	B-seal missing
R	Return accumulator damaged
S	Increased length of drill pipe
D	Abnormal damper orifice
Q	Abnormal flow in damper circuit
V	Damage to valves
O	Abnormal control line outlet
C	Abnormal high pressure accumulator

### B. Performance indicators

In this paper, accuracy, recall, precision, and F1 score are used as performance metrics for fault diagnosis of the model. Accuracy provides an overall performance evaluation; precision measures the proportion of true positive samples among those predicted to be positive by the model; recall helps to understand the model's ability to identify positive samples; and F1 score provides a single metric that balances precision and recall, which is particularly useful in unbalanced class scenarios. Higher values of accuracy, recall, F1 and precision indicate better detection performance of the model. The corresponding formulas for each metric are shown below:

$$Accuracy = \frac{TP + TN}{TP + TN + FP + FN} \quad (25)$$

$$Recall = \frac{TP}{TP + FN} \quad (26)$$

$$Precision = \frac{TP}{TP + FP} \quad (27)$$

$$F1 = 2 \times \frac{Precision \times Recall}{Precision + Recall} \quad (28)$$

where  $TP$  is the number of correctly diagnosed positive samples,  $TN$  is the number of correctly diagnosed negative samples,  $FP$  is the number of negative samples incorrectly diagnosed as positive, and  $FN$  is the number of positive samples incorrectly diagnosed as negative.

### C. Ablation experiment

This paper aims to verify the effectiveness of each model component by comparing the baseline BiLSTM and KAN models, the composite BiLSTM-KAN model, and the proposed WCBK model under noise intensities of 0.3 and 0.5. The specific performance metrics of each model are presented in



TABLE III  
PERFORMANCE INDICATORS OF ABLATION EXPERIMENT

Model	0.3 noise intensity				0.5 noise intensity			
	Accuracy	Recall	Precision	F1	Accuracy	Recall	Precision	F1
BILSTM	0.9605	0.9602	0.9603	0.9598	0.9237	0.9223	0.9229	0.9222
KAN	0.9631	0.9622	0.9625	0.9618	0.9297	0.9275	0.9271	0.9273
BILSTM-KAN	0.9691	0.9687	0.9688	0.9686	0.9394	0.9380	0.9391	0.9382
WCBK	<b>0.9714</b>	<b>0.9705</b>	<b>0.9709</b>	<b>0.9706</b>	<b>0.9450</b>	<b>0.9439</b>	<b>0.9452</b>	<b>0.9440</b>

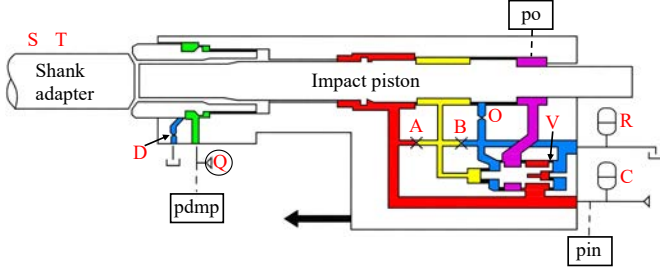


Fig. 4. Simulation of the internal structure of the drilling machine

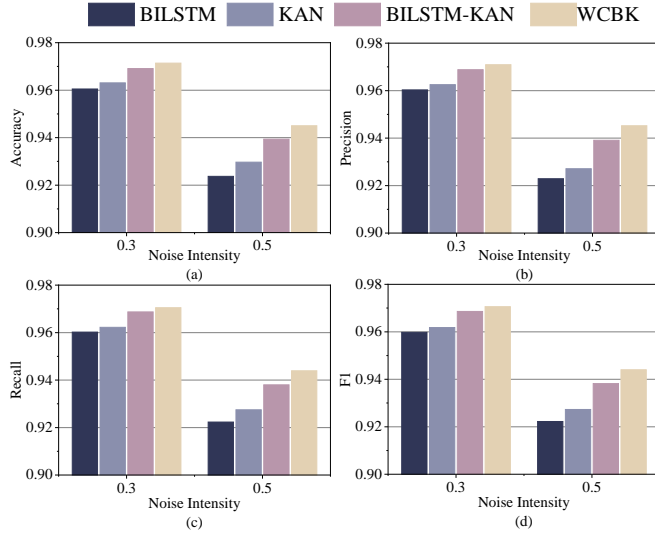


Fig. 5. Visualization of ablation experiment metrics. (a) Accuracy metric results. (b) Precision metric results. (c) Recall metric results. (d) F1 metric results.

Table III, with a visual representation of these metrics shown in Fig. 5.

Compared to the BiLSTM model, the BiLSTM-KAN composite model improves accuracy, recall, precision, and F1 by 0.0086, 0.0085, 0.0085, and 0.0088, respectively, under 0.3 intensity noise interference. Under 0.5 intensity noise interference, these metrics improve by 0.0157, 0.0157, 0.0162, and 0.016, respectively. Compared to the KAN model, the BiLSTM-KAN composite model improves accuracy, recall, precision, and F1 by 0.006, 0.0065, 0.0063, and 0.0068, respectively, under 0.3 intensity noise interference. Under 0.5 intensity noise interference, accuracy, recall, precision, and F1 are improved by 0.0097, 0.0105, 0.012, and 0.0109, respectively.

This indicates that the combination of BiLSTM and KAN

models can improve fault diagnosis accuracy under noisy interference. The bidirectional structure of the BiLSTM model allows it to capture fault features with temporal dependencies within the sequence, while the KAN model enhances flexibility by replacing weight parameters with learnable univariate functions. This adjustment helps KAN align better with fault data characteristics. Fig. 5 further shows that as the noise intensity increases, the performance metrics of the BiLSTM-KAN model improve more significantly compared to the BiLSTM and KAN models, highlighting the enhanced robustness of the composite model in noisy environments.

Compared to the composite BiLSTM-KAN model, the WCBK model demonstrates a more pronounced enhancement in performance. At a noise intensity of 0.3, the accuracy, recall, precision, and F1 scores were observed to improve by 0.0023, 0.0018, 0.0021, and 0.002, respectively. At a noise intensity of 0.5, these scores improved by 0.0056, 0.0059, 0.0061, and 0.0058, respectively. This serves to validate the effectiveness of the Wavelet Transform and Convolutional Autoencoder in noise reduction. This is because the Wavelet Transform converts time series into time-frequency images, decomposing the signal into distinct frequency bands for preliminary noise filtering. The Convolutional Autoencoder performs a further denoising process on the time-frequency images, retaining the main features while removing noise components through the learning of a low-dimensional representation of the signal. Furthermore, the model employs local connections and weight-sharing mechanisms to more effectively capture local features in the time-frequency images, thereby enhancing the denoising effect.

#### D. Individuals with different drilling machines

1) *Experiments under different noise intensities:* This paper presents an experimental investigation of the efficacy of various deep-learning architectures in predicting the noise intensity of drilling machines. The architectures include RNN, 1D-CNN, 2D-CNN, LSTM, BiLSTM, BiLSTM-KAN, Physics-guided CNN (PGCNN) [41], BO-CNN-LSTM [42], One-dimensional LSTM-residual (1D-LSTMRes) [43], and the proposed WCBK. The noise ratio applied is 0.5. The specific metrics of the experiments are presented in Table IV. In the pdmp position, the accuracy of the RNN model exhibited a gradual decrease as the noise intensity increased, with a drop from 0.9647 to 0.8637. The 1D-CNN exhibits superior recognition accuracy, reaching 0.9699 at 0.1 noise intensity and declining to 0.9022 at 0.9 noise intensity. The 2D-CNN exhibits a recognition accuracy of 0.9655 at 0.1 noise intensity

TABLE IV  
EXPERIMENTS ON DIFFERENT NOISE INTENSITIES WITH 0.5 NOISE RATIO

Position	pdmp					pin					po				
	0.1	0.3	0.5	0.7	0.9	0.1	0.3	0.5	0.7	0.9	0.1	0.3	0.5	0.7	0.9
RNN	0.9647	0.9400	0.9150	0.8843	0.8637	0.9829	0.9599	0.9266	0.8847	0.8564	0.9397	0.8566	0.8174	0.7675	0.7473
1D-CNN	0.9699	0.9576	0.9384	0.9141	0.9022	0.9629	0.9615	0.9529	0.9260	0.8898	0.9289	0.9028	0.8746	0.8174	0.7753
2D-CNN	0.9655	0.9533	0.9307	0.9166	0.9000	0.9777	0.9705	0.9613	0.9280	0.9037	0.9576	0.9047	0.8636	0.8070	0.7728
LSTM	0.9700	0.9410	0.9379	0.9123	0.8904	0.9863	0.9735	0.9518	0.9186	0.8950	0.9289	0.9077	0.8402	0.7781	0.7450
BILSTM	0.9717	0.9682	0.9598	0.9282	0.8993	0.9910	0.9857	0.9660	0.9332	0.9115	0.9742	0.9456	0.8847	0.8169	0.7860
BILSTM-KAN	0.9837	0.9752	0.9630	0.9504	0.9284	0.9912	0.9870	0.9757	0.9576	0.9396	0.9839	0.9539	0.9136	0.8686	0.8296
PGCNN	0.9751	0.9588	0.9455	0.9335	0.9134	0.9914	0.9786	0.9677	0.9400	0.9260	0.9672	0.9333	0.8842	0.8716	0.8481
BO-CNN-LSTM	0.9722	0.9585	0.9484	0.9277	0.9117	0.9905	0.9735	0.9657	0.9264	0.8857	0.9477	0.9320	0.8899	0.8388	0.6817
1D-LSTMRes	0.9685	0.9449	0.9256	0.8976	0.8728	0.9847	0.9733	0.9416	0.9094	0.8843	0.9545	0.9035	0.8515	0.7932	0.7467
WCBK	<b>0.9876</b>	<b>0.9822</b>	<b>0.9750</b>	<b>0.9644</b>	<b>0.9584</b>	<b>0.9932</b>	<b>0.9883</b>	<b>0.9784</b>	<b>0.9686</b>	<b>0.9445</b>	<b>0.9874</b>	<b>0.9669</b>	<b>0.9426</b>	<b>0.9081</b>	<b>0.8656</b>

and 0.9004 at 0.9 noise intensity. The LSTM exhibits superior recognition accuracy under low noise intensity, reaching 0.9700, and shows a decrease to 0.8993 at 0.9 noise intensity. The BILSTM's recognition accuracy decreases from 0.9717 to 0.9086. The BILSTM-KAN model demonstrates a more gradual decrease in accuracy with increasing noise intensity, from 0.9837 to 0.9294. The PGCNN model demonstrates minimal variation in accuracy, with a slight decrease from 0.9751 to 0.9134. The BO-CNN-LSTM model exhibits an accuracy of 0.9722 at 0.1 noise intensity and 0.9171 at 0.9 noise intensity. The accuracy of the 1D-LSTMRes model decreases from 0.9685 to 0.8941. The WCBK model exhibits the highest accuracy, decreasing from 0.9876 to 0.9584, demonstrating excellent robustness.

In the pin position, the accuracy of the RNN model exhibited a decrease, from 0.9829 to 0.9397. The 1D-CNN exhibits an accuracy of 0.9629 at 0.1 noise intensity and 0.9289 at 0.9 noise intensity. The accuracy of the 2D-CNN decreases from 0.9684 to 0.9392. The LSTM demonstrates superior performance at low noise intensities, achieving an accuracy of 0.9731. However, at 0.9 noise intensity, its accuracy decreases to 0.9408. The BILSTM exhibited a decrease in accuracy, from 0.9790 to 0.9442. The accuracy of the BILSTM-KAN model decreases from 0.9887 to 0.9600. The PGCNN's accuracy decreases from 0.9810 to 0.9566. The BO-CNN-LSTM model exhibits an accuracy of 0.9847 at 0.1 noise intensity and 0.9630 at 0.9 noise intensity. The accuracy of the 1D-LSTMRes model decreases from 0.9702 to 0.9440. The WCBK model exhibits the highest accuracy, decreasing from 0.9932 to 0.9686, demonstrating exceptional robustness.

In the po position, the accuracy of the RNN decreases from 0.9829 to 0.7473. The 1D-CNN exhibits an accuracy of 0.9629 at 0.1 noise intensity and 0.7753 at 0.9 noise intensity. The accuracy of the 2D-CNN model exhibited a notable decrease, from 0.9684 to 0.7853. The LSTM demonstrates superior performance under low noise intensity, achieving an accuracy of 0.9731. However, at 0.9 noise intensity, its accuracy decreases to 0.7792. The BILSTM exhibited a notable decrease from 0.9790 to 0.7790 in accuracy. The accuracy of the BILSTM-KAN model decreases from 0.9887 to 0.8686. The PGCNN's accuracy exhibits a decrease from 0.9810 to 0.8174. The BO-CNN-LSTM model exhibits an accuracy of 0.9847 at 0.1 noise intensity and 0.8481 at 0.9 noise intensity. The accuracy of the 1D-LSTMRes model decreases from 0.9702 to 0.7540. The

WCBK model exhibits the highest accuracy, decreasing from 0.9932 to 0.8656, demonstrating excellent robustness.

The WCBK model exhibits the highest accuracy and strongest robustness across different noise intensities, particularly maintaining high accuracy under higher noise intensities. In contrast, traditional RNN and LSTM models exhibit a notable decline in performance when subjected to high noise intensity. However, composite models like BILSTM-KAN and WCBK demonstrate robust resilience to noise. This underscores the benefits of the WCBK model in noise filtration and feature extraction.

As shown in Table V, the overall accuracy of all models tends to decrease as the noise intensity increases. However, at a noise intensity of 0.9, the WCBK model maintains a high accuracy of 0.7945 on the PD dataset, which is at least 0.07 higher than that of the other models. This highlights the model's excellent noise suppression capability. The WCBK model also outperforms others on the PDMP dataset, demonstrating its ability to capture and optimize the dataset's intrinsic features more effectively. Compared to traditional models such as LSTM and BILSTM, advanced composite models like WCBK offer better adaptability and performance. In particular, for nonlinear and non-stationary signals, a single model may fail to capture all relevant features, whereas composite models, by integrating multiple techniques, can provide a more comprehensive analysis. The WCBK model consistently performs well across various noise intensities and dataset parts, while other models, like 2D-CNN, show suboptimal performance at specific noise levels or sections. This indicates the superior robustness and generalization ability of the WCBK model. The WCBK model combines Wavelet Transform and Convolutional Autoencoders for noise removal, along with BILSTM and KAN networks. This combination is key to its strong performance in high-noise environments. Wavelet Transform effectively separates noise components from the signal, while Convolutional Autoencoders learn deep feature representations, facilitating more accurate signal reconstruction. BILSTM captures long-term dependencies in time series data, and KAN processes critical fault features, enabling high-precision fault diagnosis even under noise interference.

2) *Experiments with different noise ratios*: This study employs a series of experiments to assess the performance of various neural network models under varying noise ratios. The models included in this investigation are RNN, 2D-

TABLE V  
EXPERIMENTS ON DIFFERENT NOISE INTENSITIES WITH 1 NOISE RATIO

Position	pdmp					pin					po				
	0.1	0.3	0.5	0.7	0.9	0.1	0.3	0.5	0.7	0.9	0.1	0.3	0.5	0.7	0.9
RNN	0.9257	0.9295	0.8906	0.8477	0.8117	0.9765	0.9415	0.9019	0.8501	0.8053	0.9218	0.8548	0.7632	0.6651	0.5984
1D-CNN	0.9643	0.9534	0.9292	0.8991	0.8822	0.9460	0.9555	0.9358	0.9032	0.8448	0.8641	0.8533	0.8108	0.7473	0.6886
2D-CNN	0.9636	0.9487	0.9221	0.9001	0.8830	0.9831	0.9647	0.9404	0.8909	0.8764	0.9296	0.8847	0.8210	0.7390	0.6873
LSTM	0.9660	0.9383	0.9169	0.8858	0.8520	0.9557	0.9430	0.9398	0.8891	0.8397	0.9705	0.8691	0.7997	0.7070	0.6351
BILSTM	0.9759	0.9605	0.9237	0.8913	0.8763	0.9886	0.9787	0.9387	0.9109	0.8865	0.9705	0.9270	0.8379	0.7401	0.6786
BILSTM-KAN	0.9826	0.9691	0.9394	0.9082	0.8690	0.9912	0.9816	0.9567	0.9225	0.8832	0.9783	0.9453	0.8590	0.7764	0.7245
PGCNN	0.9822	0.9633	0.9448	0.9189	0.8968	<b>0.9924</b>	0.9801	0.9596	0.9396	0.8940	0.9698	0.9304	0.8322	0.7918	0.7176
BO-CNN-LSTM	0.9660	0.9444	0.9269	0.8858	0.8760	0.9557	0.9709	0.9441	0.8891	0.8857	0.9705	0.9071	0.8159	0.7573	0.6817
1D-LSTMRes	0.9616	0.9431	0.8995	0.8699	0.8312	0.9808	0.9589	0.9259	0.8837	0.8391	0.9440	0.8790	0.8136	0.7146	0.6297
WCBK	<b>0.9883</b>	<b>0.9714</b>	<b>0.9624</b>	<b>0.9432</b>	<b>0.9190</b>	0.9922	<b>0.9871</b>	<b>0.9762</b>	<b>0.9522</b>	<b>0.9137</b>	<b>0.9885</b>	<b>0.9623</b>	<b>0.8991</b>	<b>0.8264</b>	<b>0.7945</b>

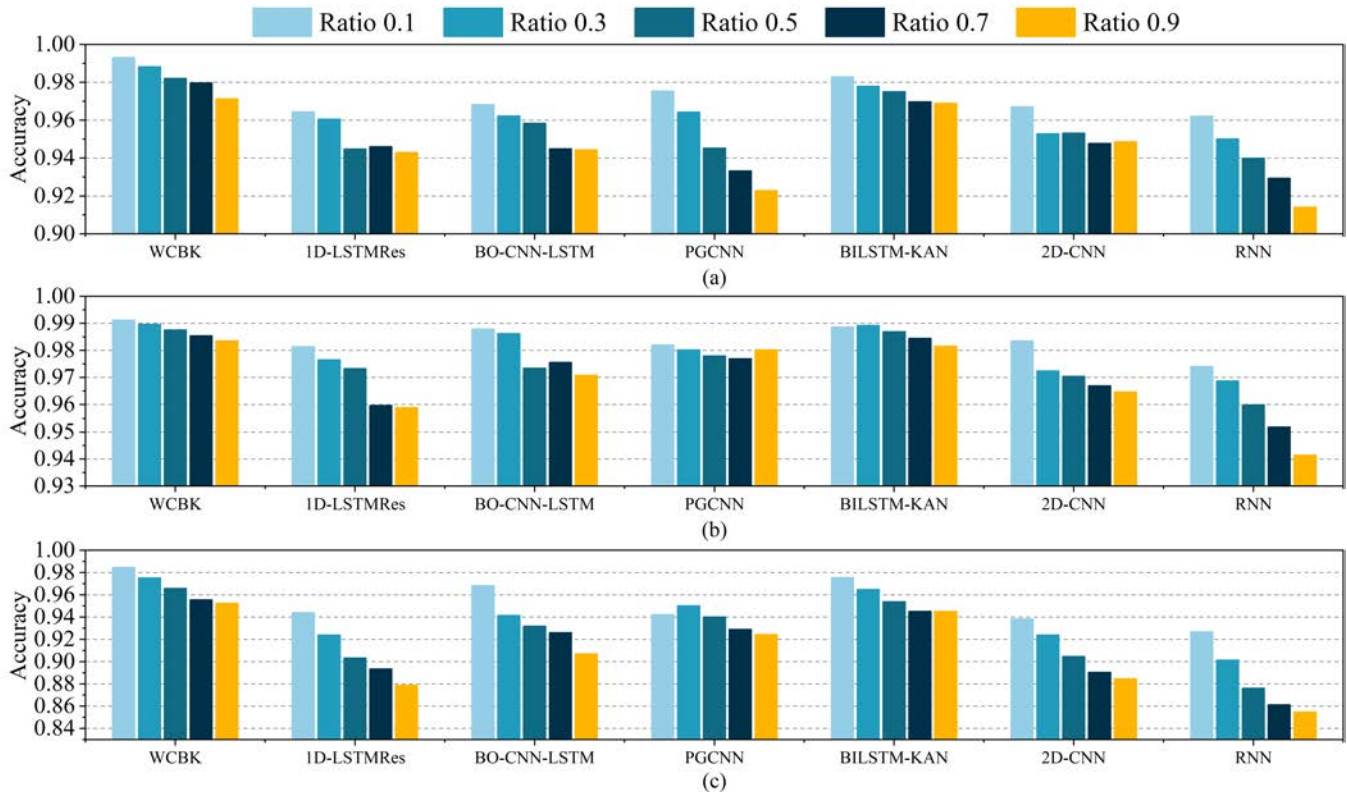


Fig. 6. Noise intensity 0.3 visualizations of accuracy metrics for each model at different noise ratios. (a) Results in the pdmp position. (b) Results in the pin position. (c) Results in the po position.

CNN, KAN, BILSTM-KAN, PGCNN, BO-CNN-LSTM, 1D-LSTMRes, and WCBK. Fig. 6 and Fig.8 depict the accuracy metrics of each model under 0.3 and 0.7 noise intensity, respectively. Fig. 6 illustrates that, at lower noise intensities, the performance of each model is relatively robust. However, as the noise ratio increases, the performance of some models declines only slightly.

Fig. 7 depicts a notable decline in the recognition accuracy of each model in comparison to Fig. 6, which illustrates the general performance degradation of models under higher noise intensities. This phenomenon reflects the differences in robustness and adaptability of the models when confronted with varying levels of noise interference.

In the context of low noise ratios (0.1 and 0.3), the 1D-LSTMRes model demonstrates a commendable performance, sustaining a high degree of fault diagnosis accuracy. This is

because, in low-noise environments, the model can effectively capture the essential features of the time series. However, as the noise ratio increases, the performance of the 1D-LSTMRes model exhibits a notable decline, with accuracy decreasing significantly. Higher noise ratios impede the extraction of features from the time series, thereby constraining the model's capacity for prediction.

At medium noise ratios (0.3 and 0.5), the BO-CNN-LSTM model demonstrates satisfactory performance, maintaining high accuracy in fault diagnosis. This is due to the model combining the strengths of CNN and LSTM networks, with Bayesian Optimization fine-tuning the hyperparameters, thereby enhancing the model's adaptability under moderate noise conditions. Nevertheless, at elevated noise ratios (0.7 and 0.9), the accuracy of the BO-CNN-LSTM model markedly declines, indicating diminished adaptability to high-noise en-

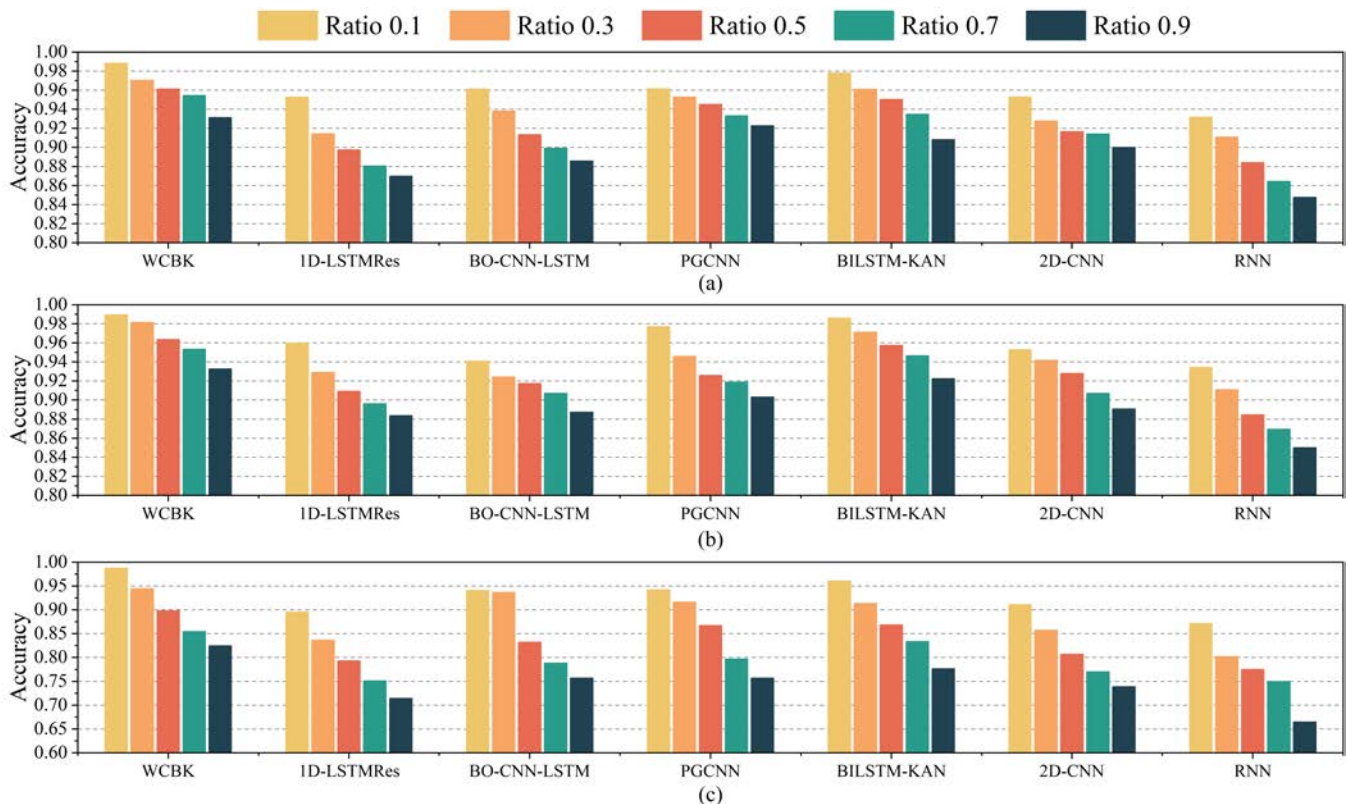


Fig. 7. Noise intensity 0.7 visualizations of accuracy metrics for each model at different noise ratios. (a) Results in the pdmp position. (b) Results in the pin position. (c) Results in the po position.

vironments. This may be attributed to the interference of noise with the efficacy of convolutional feature extraction and time dependency capture.

As the noise ratio rises, the PGCNN model's accuracy declines markedly, indicating a high degree of sensitivity to noise. The PGCNN model demonstrates satisfactory performance under low noise ratios. However, its capacity for recognition rapidly diminishes as the noise ratio increases. This suggests that the model is susceptible to performance degradation in high-noise environments, as the presence of noise impairs the model's capacity to extract features from graph-structured data.

The BiLSTM-KAN model demonstrates relatively consistent performance across varying noise ratios, exhibiting a comparatively smaller decline in accuracy compared to other models. This model fuses the capabilities of the KAN and BiLSTM, enabling the capture of intricate nonlinear relationships and time series dependencies within the data. Even in high-noise environments, it demonstrates a relatively high level of fault diagnosis accuracy, indicating robust noise resistance and adaptability.

The accuracy of the 2D-CNN model is markedly diminished with the escalation of noise ratios, exhibiting pronounced deficiencies at elevated noise ratios (0.7 and 0.9). While the 2D-CNN model has certain advantages in processing image data, its feature extraction capability is significantly impaired in high-noise environments, resulting in a notable decline in recognition performance. This demonstrates the inadequate

resilience of the 2D-CNN model in the presence of noise interference.

The RNN model exhibits the poorest performance across all noise ratios, with accuracy rapidly declining as the noise ratio increases, indicating weak noise resistance. The RNN has limited capacity in handling time series data and is susceptible to disruption by noise, rendering it ineffective in recognizing fault features in high-noise environments. This illustrates the significantly poor adaptability of the RNN model in high-noise environments.

The WCBK model demonstrates optimal performance across all noise ratios, maintaining superior accuracy compared to other models even at the highest noise ratio of 0.9, which reflects its robust noise resistance. This is due to the Wavelet Transform's ability to effectively separate noise components from fault features, thereby suppressing high-frequency noise. Convolutional Autoencoders learn low-dimensional representations of the data, removing noise while retaining important fault features, enabling the model to extract effective features even in high-noise environments. The BiLSTM network captures long-term dependencies and dynamic features in time series data, which remain effective even under noisy conditions. The KAN model excels at identifying intricate nonlinear relationships within the data, crucial for recognizing complex patterns in fault diagnosis. As a result, the WCBK model achieves consistent and reliable fault diagnosis accuracy, even in the presence of high noise intensities.

TABLE VI  
ACCURACY METRICS FOR DIFFERENT NOISE INTENSITIES AT 0.5 SCALE

Noise intensity	Machine 1					Machine 5				
	0.1	0.3	0.5	0.7	.0.9	0.1	0.3	0.5	0.7	0.9
RNN	0.9416	0.8998	0.8710	0.8253	0.8187	0.8184	0.7648	0.7108	0.6741	0.6525
1D-CNN	0.9479	0.9207	0.8934	0.8706	0.8600	0.8651	<b>0.8320</b>	0.7867	0.7530	0.7199
2D-CNN	0.9420	0.9124	0.8853	0.8601	0.8495	0.8861	0.8267	0.7837	0.7360	0.7211
LSTM	0.9241	0.8771	0.8306	0.8169	0.7441	0.8492	0.8095	0.7603	0.7147	0.6960
BILSTM	0.9454	0.9094	0.8860	0.8691	0.8540	0.8217	0.8045	0.7465	0.7165	0.6896
BILSTM-KAN	0.9575	<b>0.9239</b>	<b>0.8996</b>	0.8739	0.8461	0.8754	0.7967	0.7737	0.7352	0.7187
PGCNN	0.9523	0.9120	0.8903	0.8690	0.8502	0.8381	0.8049	0.7917	0.7530	0.7179
BO-CNN-LSTM	0.9485	0.8818	0.8771	0.8560	0.8169	<b>0.8828</b>	0.7919	0.7456	0.7246	0.7092
1D-LSTMRes	0.9342	0.8825	0.8564	0.8290	0.8050	0.8201	0.7840	0.7354	0.6783	0.6392
WCBK	<b>0.9491</b>	0.9210	0.8934	<b>0.8835</b>	<b>0.8749</b>	0.8682	0.8191	<b>0.7977</b>	<b>0.7574</b>	<b>0.7446</b>

### E. Experiments between different positions of the drilling machine

1) *Experiments under different noise intensities:* This paper selects the RNN, 1D-CNN, 2D-CNN, LSTM, BILSTM, BILSTM-KAN, PGCNN, BO-CNN-LSTM, 1D-LSTMRes, and WCBK models to conduct experiments on various parts of the drilling machine. The pressure data from three different sections of Machines 1 and 5 serve as the experimental dataset. Comparative experiments are performed under different noise intensities with noise ratios of 0.5 and 1. The specific experimental metrics are presented in Tables VI and VII.

At a noise ratio of 0.5, the accuracy of the RNN model on the Machine 1 dataset exhibited a notable decline as the noise intensity increased from 0.2 to 1, with the accuracy dropping from 0.9416 to 0.8177. Similarly, on the Machine 5 dataset, the RNN model demonstrated a significant reduction in accuracy, falling from 0.8184 to 0.6525 as the noise intensity increased. As the noise ratio increases to 1, the RNN model's performance declines even more significantly, indicating a lack of resilience to noise.

In the Machine 1 dataset at a 0.5 noise ratio, the accuracy of the 2D-CNN model is observed to decline from 0.9420 to 0.8945. At a noise ratio of 1, the performance metrics demonstrate a further decline, indicating that while the 2D-CNN has some capacity to handle noise, it is less effective at higher noise levels. The LSTM model's accuracy declines from 0.9241 to 0.7441, indicating a lack of resilience to noise. Despite its proficiency in processing time series data, high noise intensity impedes the LSTM's ability to extract fault features.

In comparison to the LSTM model, the BILSTM model demonstrates a relatively stable performance, indicating an enhanced capacity to resist noise interference. The BILSTM's bidirectional structure facilitates the capture of bidirectional dependencies in time series data, thereby reducing the impact of noise. The BILSTM-KAN model exhibits superior performance compared to the BILSTM model at both noise ratios of 0.5 and 1. This is attributed to the fact that the BILSTM-KAN integrates the capture of bidirectional time series features with the modeling of complex nonlinear relationships, effectively addressing noise interference and extracting crucial fault features. In the Machine 1 dataset at a 0.5 noise ratio, it can be observed that the PGCNN model's accuracy undergoes

a decline, from 0.9523 to 0.8502. At a 1 noise ratio on the Machine 5 dataset, the model's performance drops from 0.8762 to 0.6491, indicating that composite neural network models are more robust in high-noise environments than single neural network structures.

In the Machine 1 dataset at a 0.5 noise ratio, the BO-CNN-LSTM model's accuracy decreases from 0.9485 to 0.8169, indicating a satisfactory level of performance. The application of Bayesian optimization enables the BO-CNN-LSTM to maintain a high level of accuracy in the presence of moderate noise intensities. The 1D-LSTMRes model demonstrates robust performance at low noise intensities but exhibits a notable decline at high noise intensities.

The WCBK model exhibits the most comprehensive performance across a range of machines and noise intensities. This is because the WCBK model incorporates Wavelet Transform and Convolutional Autoencoder denoising techniques, which are capable of effectively separating and removing noise at different frequencies. Furthermore, the integration of the BILSTM-KAN composite neural network offers substantial benefits in the processing of intricate noise and the extraction of pivotal features.

2) *Experiments with different noise ratios:* Figs. 8 and 9 demonstrate the degree of accuracy variation among different models on the Machine 1 and Machine 5 datasets when subjected to varying noise ratios (0.2, 0.4, 0.6, 0.8, 1.0) at noise intensities of 0.3 and 0.9. Figs. 8(a) and 9(a) depict the Machine 1 dataset, while Figs. 8(b) and 9(b) illustrate the Machine 5 dataset. The performance of each model is represented by a distinct color line. In general, the WCBK and BILSTM-KAN models exhibit excellent performance across a range of noise ratios, demonstrating the strongest resilience to noise. The accuracy of these two models remains consistently high and declines only slightly as the noise ratio increases, demonstrating outstanding performance.

The BILSTM and 2D-CNN models demonstrate a relatively gradual decline in accuracy, indicating a certain level of noise resistance. Although accuracy declines with increasing noise ratios, it remains relatively high at higher noise ratios.

The accuracy of the RNN and 1D-LSTMRes models is significantly reduced with increasing noise ratios, indicating a high degree of sensitivity to noise. These models demonstrate the most pronounced decline in accuracy at elevated noise



TABLE VII  
ACCURACY METRICS FOR DIFFERENT NOISE INTENSITIES AT 0.7 SCALE

Noise intensity	Machine 1					Machine 5				
	0.1	0.3	0.5	0.7	.0.9	0.1	0.3	0.5	0.7	0.9
RNN	0.9139	0.8612	0.8114	0.7675	0.7357	0.8029	0.7192	0.6550	0.5710	0.5385
1D-CNN	0.9105	0.8722	0.8422	0.8132	0.6703	0.8238	0.7590	0.7321	0.6703	0.6555
2D-CNN	0.9285	0.8844	0.8517	0.8204	0.7986	0.8556	0.7900	0.7339	0.6787	0.6496
LSTM	0.9084	0.8635	0.8347	0.7981	0.7744	0.8108	0.7511	0.6764	0.6326	0.5905
BILSTM	0.9236	0.8827	0.8354	0.8062	0.7805	0.8075	0.7602	0.6959	0.6434	0.6017
BILSTM-KAN	0.9257	0.8688	0.8277	0.7939	0.7658	0.7364	0.7259	0.6730	0.6145	0.5690
PGCNN	<b>0.9405</b>	0.8823	0.8538	<b>0.8502</b>	<b>0.8236</b>	<b>0.8762</b>	0.7928	0.7369	0.6696	0.6491
BO-CNN-LSTM	0.9347	0.8602	0.8411	0.8136	0.7958	0.8085	0.7260	0.7063	0.6460	0.6197
1D-LSTMRes	0.8932	0.8510	0.8083	0.7678	0.7400	0.7810	0.7106	0.6421	0.5858	0.5457
WCBK	0.9321	<b>0.8848</b>	<b>0.8583</b>	0.8396	0.8185	0.8472	<b>0.7995</b>	<b>0.7731</b>	<b>0.7139</b>	<b>0.6944</b>

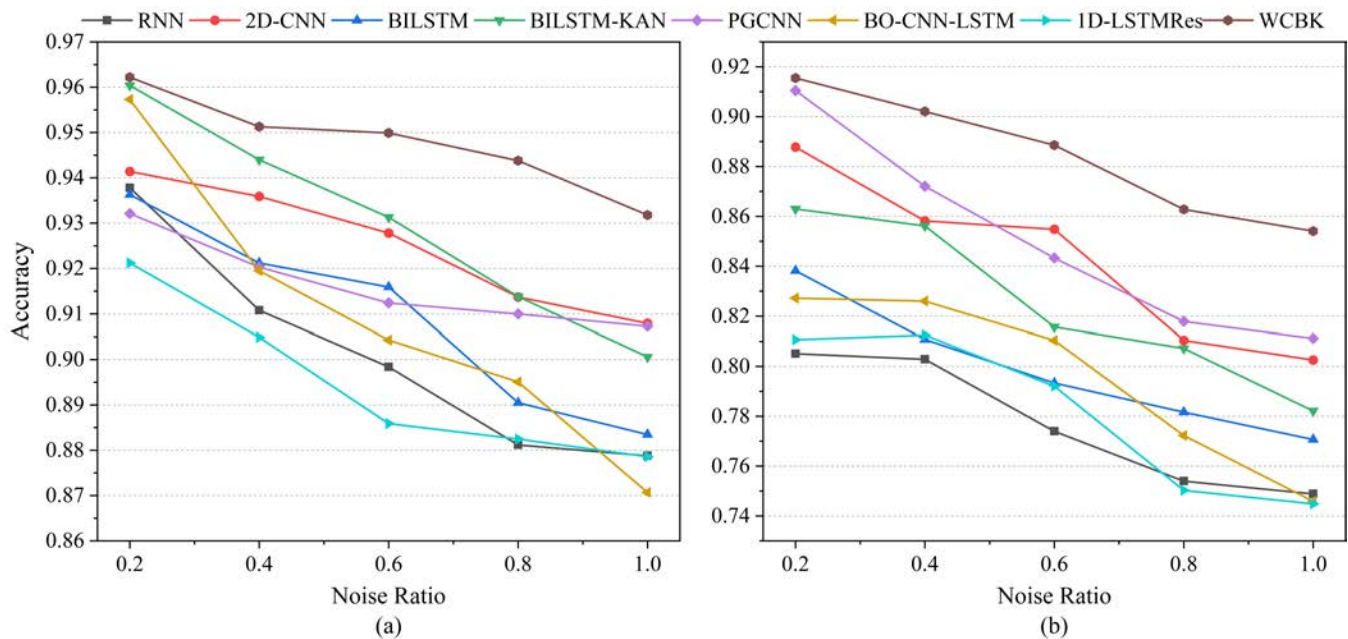


Fig. 8. The proportion of different noises at noise intensity is 0.3. (a) Dataset for different positions of machine 1. (b) Dataset for different positions of machine 5.

ratios, indicating a lack of resilience to high levels of noise.

The PGCNN and BO-CNN-LSTM models demonstrate satisfactory performance at moderate noise ratios but exhibit a notable decline in accuracy at high noise ratios, indicating average adaptability. These models demonstrate high accuracy at low to moderate noise ratios but exhibit poor performance at high noise ratios.

In the comprehensive examination, the RNN model demonstrates a notable reduction in accuracy on both machines, suggesting a high degree of sensitivity to noise. The 2D-CNN model initially exhibits high accuracy but subsequently demonstrates a gradual decline in performance as noise ratios increase. However, it does exhibit some resilience to noise. The BILSTM model demonstrates a relatively stable performance at high noise ratios, indicating good noise resistance. The BILSTM-KAN model demonstrates consistent accuracy across all noise ratios, indicating excellent noise resistance. The PGCNN and BO-CNN-LSTM models demonstrate a notable decline in performance at elevated noise ratios, indicating a discernible impact of noise. The 1D-LSTMRes model exhibits

a notable decline in accuracy with elevated noise ratios, indicative of its high sensitivity to noise. The WCBK model exhibits the highest accuracy across all noise ratios, thereby demonstrating the most robust noise resistance. The exceptional performance of the WCBK model can be attributed to its multi-level and multi-modal feature extraction and fusion mechanisms, along with its robust time-series processing and nonlinear modeling capabilities. The denoising capabilities of the Wavelet Transform and Convolutional Autoencoders, the time-series feature capturing of the BILSTM, and the nonlinear mapping capability of KAN, when combined with comprehensive feature fusion and robust training strategies, enable the WCBK model to maintain high accuracy under various noise conditions, thereby demonstrating outstanding noise resistance.

#### F. Model adaptation experiments

This paper employs a noise ratio of 1 and a noise intensity of 0.3 to investigate the adaptability of diverse models for fault

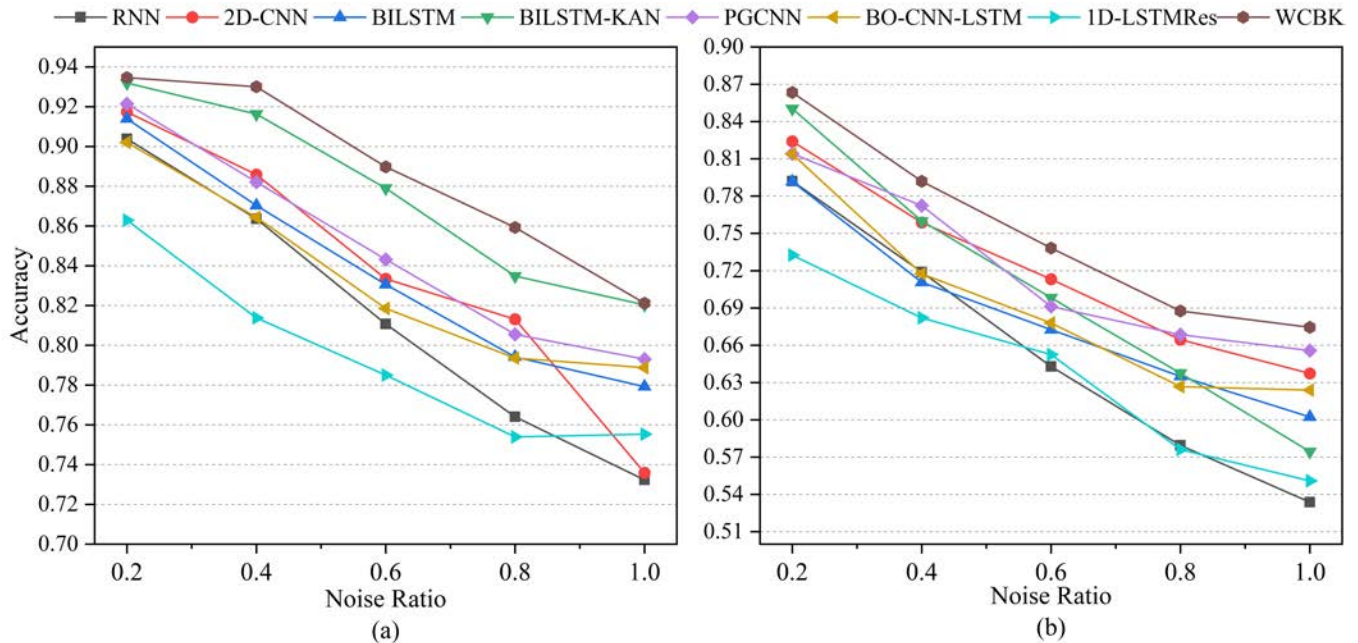


Fig. 9. Proportion of different noises at noise intensity 0.9. (a) Dataset for different positions of machine 1. (b) Dataset for different positions of machine 5.

TABLE VIII  
MODEL ADAPTATION ACCURACY METRICS FOR A NOISE SCALE OF 1 AND INTENSITY OF 0.3

Machine	pdmp					pin					po				
	1	2	3	4	5	1	2	3	4	5	1	2	3	4	5
RNN	0.4084	0.2800	0.5304	0.4899	0.4770	0.3617	0.4984	0.7246	0.8594	0.7710	0.3383	0.3907	0.4571	0.7951	0.6450
1D-CNN	0.4883	0.3756	0.5783	0.5245	0.4776	0.4095	<b>0.6926</b>	0.7406	0.8667	0.6501	0.3474	0.5495	0.6237	0.8276	0.7467
2D-CNN	0.5300	0.4213	0.6227	0.5330	0.4333	0.4253	0.6037	0.7226	0.8731	<b>0.7953</b>	0.2712	0.5076	0.6127	0.8785	0.7102
LSTM	0.4543	0.3093	0.5740	0.4833	0.5031	0.3295	0.4930	0.6971	0.8612	0.6386	0.2791	0.3203	0.3573	0.7848	0.6264
BILSTM	0.4190	0.3698	0.7109	0.4871	0.5168	0.3063	0.5917	0.6532	0.8469	0.5742	0.2977	0.3363	0.4380	0.7767	0.6349
BILSTM-KAN	0.5155	0.3625	0.6900	0.4657	<b>0.5229</b>	0.3134	0.5129	0.6957	0.8460	0.6991	0.3501	0.3512	0.4566	0.7385	0.6592
PGCNN	0.5062	0.4260	0.6327	0.5801	0.5198	0.4324	0.6916	0.7485	0.8930	0.7467	0.4086	0.5045	0.6348	0.8656	0.7175
BO-CNN-LSTM	<b>0.5467</b>	0.5204	0.6101	0.5173	0.4785	0.3645	0.5834	0.7267	0.8366	0.7160	0.4219	0.4793	0.6011	0.8242	0.7610
1D-LSTMRes	0.4483	0.3293	0.6288	0.4965	0.4652	0.3059	0.5638	0.7263	0.8657	0.7528	0.2436	0.3822	0.4683	0.8105	0.6832
WCBK	0.4305	<b>0.5739</b>	<b>0.7853</b>	<b>0.6854</b>	0.4962	<b>0.4724</b>	0.6524	<b>0.8770</b>	<b>0.9053</b>	0.6744	<b>0.5458</b>	<b>0.6059</b>	<b>0.7385</b>	<b>0.8883</b>	<b>0.7767</b>

diagnosis in a range of drilling machines. The data from five machines are divided into three distinct categories for analysis. Machines 1, 2, 3, 4, and 5 are employed as test sets, while the remaining data are utilized as a training set to assess the adaptability of each model to diverse drilling machine fault diagnoses. The specific performance metrics of each model are presented in Table VIII.

In the pdmp dataset, the RNN model demonstrates considerable variability in accuracy across the test sets, with a range of 0.28 to 0.5304, suggesting instability. The 1D-CNN model demonstrates relatively balanced accuracy, although it performs less well on test set 3. The 2D-CNN model demonstrates stability, although its accuracy on test sets 2 and 3 is relatively low. The LSTM model demonstrates the most optimal performance on test set 3, with an accuracy of 0.574, while exhibiting moderate performance on the other test sets. The BILSTM model demonstrates a relatively balanced performance, attaining the highest accuracy of 0.7109 on test set 3. The BILSTM-KAN model demonstrates remarkable performance, particularly on test set 5, attaining the highest accuracy of 0.5229 and outperforming all other comparison

models. The PGCNN model demonstrates overall performance that is above average, achieving the highest accuracy of 0.6327 on test set 3. The BO-CNN-LSTM model exhibits the highest accuracy of 0.6101 on test set 3 while demonstrating relatively balanced performance on the remaining test sets. The 1D-LSTMRes model demonstrates average performance across all metrics. The WCBK model demonstrates exemplary performance on test sets 2, 3, and 4, attaining the most favorable performance metrics, particularly achieving the highest accuracy of 0.7853 on test set 3.

In the pin dataset, the RNN model demonstrates suboptimal performance on test set 1, with an accuracy of 0.36. Conversely, it exhibits superior performance on test set 5, achieving an accuracy of 0.771. The 1D-CNN model demonstrated the highest level of accuracy on test set 2, with a score of 0.69, outperforming all other models. The 2D-CNN model demonstrates remarkable performance on test set 4, exhibiting above-average results on other test sets. The LSTM model demonstrates the highest level of accuracy on test set 4, with a score of 0.7848, indicating a relatively balanced overall performance. The BILSTM model exhibits



suboptimal performance on test set 1, with an accuracy of 0.3063. Conversely, it demonstrates superior performance on test set 4, achieving an accuracy of 0.8469. The BILSTM-KAN model demonstrates remarkable overall performance, attaining the highest accuracy of 0.846 on test set 4. The PGCNN model demonstrates the highest performance on test set 4, achieving 0.893 and exhibiting above-average overall performance. The BO-CNN-LSTM model demonstrates the highest accuracy on test set 4, with a score of 0.8366, while exhibiting average performance on the remaining test sets. The 1D-LSTMRes model demonstrates satisfactory performance on test set 2, with an accuracy of 0.75, indicating average overall performance. The WCBK model demonstrates balanced and excellent performance across all test sets, particularly achieving the highest accuracy among all models on test sets 1, 3, and 4.

In the po dataset, the RNN model demonstrates suboptimal performance on test set 1, with an accuracy of 0.3383. Conversely, it exhibits superior performance on test set 4, achieving an accuracy of 0.7951. The 1D-CNN model demonstrates a noteworthy performance on test set 4, with an accuracy of 0.8276. However, its performance on other test sets is more average. The 2D-CNN model attains the highest level of accuracy, 0.8785, on test set 4. The LSTM model demonstrates satisfactory performance on test set 3, with an accuracy of 0.78, indicating an average overall performance. The BILSTM model exhibited the highest accuracy on test set 4, with a accuracy of 0.7767. The BILSTM-KAN model demonstrates overall efficacy, attaining the highest accuracy of 0.7385 on test set 4. The PGCNN model exhibits the highest performance on test set 4, achieving 0.8656, and demonstrates above-average overall performance. The BO-CNN-LSTM model demonstrated the highest accuracy of 0.8242 on test set 4, while exhibiting average performance on the remaining test sets. The 1D-LSTMRes model demonstrates satisfactory performance on test set 4, with an accuracy of 0.8105, indicating average overall performance. The WCBK model demonstrates balanced and excellent performance on all test sets, particularly achieving the highest accuracy of 0.8883 on test set 4.

The WCBK model exhibits balanced and excellent performance across all test sets and dataset types, indicating strong adaptability and robustness. The WCBK model's combination of Wavelet Transform, Convolutional Autoencoders, BILSTM, and KAN networks forms a multi-level, multi-dimensional feature extraction and analysis framework, exhibiting remarkable adaptability and robustness. The model is capable of adapting to signal features of varying frequencies and time scales, handling complex time series dependencies, modeling nonlinear and high-dimensional data, and maintaining high performance even in noisy environments.

## VI. CONCLUSION

This paper proposes and validates an innovative fault diagnosis model, WCBK, for drilling machines that aims to improve the accuracy of fault diagnosis under complex working conditions. The main contribution of this model is its

ability to maintain fault diagnosis capability under strong noise interference. The Wavelet Transform is used to decompose input signals into the time-frequency domain, effectively extracting key fault features and reducing noise interference. The Convolutional Autoencoder then processes these features, focusing on retaining fault-related information. To enhance analytical capacity, BILSTM captures long-term dependencies and temporal dynamics in the fault data. The KAN dynamically highlights key features, improving both interpretability and attention to critical information. The integration of BILSTM and KAN strengthens the model's ability to analyze and classify fault patterns accurately. The effectiveness of the model is verified through ablation experiments, different individual experiments, different part experiments, and model adaptability experiments.

Although the WCBK model demonstrates good fault diagnosis performance under strong noise interference, its performance may vary under different operating conditions. Therefore, future research can explore ways to further enhance the model's generalization ability to ensure it maintains efficient fault diagnosis performance in more complex and variable working environments. Techniques such as transfer learning can be employed to enable the model to quickly adapt to new operating conditions or equipment types, thereby improving its adaptability and robustness in different scenarios.

## REFERENCES

- [1] T. H. Son, Z. Weedon, T. Yigitcanlar, T. Sanchez, J. M. Corchado, and R. Mehmood, "Algorithmic urban planning for smart and sustainable development: Systematic review of the literature," *Sustainable Cities and Society*, vol. 94, p. 104562, 2023.
- [2] X. Li, L. Ma, A. M. Ruman, N. Iqbal, and W. Strielkowski, "Impact of natural resource mining on sustainable economic development: The role of education and green innovation in china," *Geoscience Frontiers*, vol. 15, no. 3, p. 101703, 2024.
- [3] J. Cai, T. Liu, T. Wang, H. Feng, K. Fang, A. K. Bashir, and W. Wang, "Multi-source fusion enhanced power-efficient sustainable computing for air quality monitoring," *IEEE Internet of Things Journal*, 2024.
- [4] K. Fang, T. Wang, X. Zhou, Y. Ren, H. Guo, and J. Li, "A topsis-based relocalization algorithm in wireless sensor networks," *IEEE Transactions on Industrial Informatics*, vol. 18, no. 2, pp. 1322–1332, 2021.
- [5] Y. Luo, M. R. Abidian, J.-H. Ahn, D. Akinwande, A. M. Andrews, M. Antonietti, Z. Bao, M. Berggren, C. A. Berkey, C. J. Bettinger *et al.*, "Technology roadmap for flexible sensors," *ACS nano*, vol. 17, no. 6, pp. 5211–5295, 2023.
- [6] S. K. S. Tyagi, W. Wei, V. Piuri, S. C. Mukhopadhyay, A. Striegel, O. Elloumi, S. Zeadally, W. Wang, and N. Kumar, "Guest editorial special issue on artificial intelligence-based sensors for next generation iot applications," *IEEE Sensors Journal*, vol. 21, no. 22, pp. 24919–24919, 2021.
- [7] K. Fang, T. Wang, L. Tong, X. Fang, Y. Pan, W. Wang, and J. Li, "Non-intrusive security assessment methods for future autonomous transportation iot," *IEEE Transactions on Automation Science and Engineering*, vol. 21, no. 3, pp. 2387–2399, 2024.
- [8] S. A. Mansouri, A. R. Jordehi, M. Marzband, M. Tostado-Véliz, F. Jurado, and J. A. Aguado, "An iot-enabled hierarchical decentralized framework for multi-energy microgrids market management in the presence of smart prosumers using a deep learning-based forecaster," *Applied Energy*, vol. 333, p. 120560, 2023.
- [9] T. Wang, J. Li, W. Wei, W. Wang, and K. Fang, "Deep-learning-based weak electromagnetic intrusion detection method for zero touch networks on industrial iot," *IEEE Network*, vol. 36, no. 6, pp. 236–242, 2022.
- [10] H. Shao, W. Li, B. Cai, J. Wan, Y. Xiao, and S. Yan, "Dual-threshold attention-guided gan and limited infrared thermal images for rotating machinery fault diagnosis under speed fluctuation," *IEEE Transactions on Industrial Informatics*, vol. 19, no. 9, pp. 9933–9942, 2023.

- [11] H. Feng, Q. Li, W. Wang, A. K. Bashir, A. K. Singh, J. Xu, and K. Fang, "Security of target recognition for uav forestry remote sensing based on multi-source data fusion transformer framework," *Information Fusion*, vol. 112, p. 102555, 2024.
- [12] K. Fang, T. Wang, X. Yuan, C. Miao, Y. Pan, and J. Li, "Detection of weak electromagnetic interference attacks based on fingerprint in iiot systems," *Future Generation Computer Systems*, vol. 126, pp. 295–304, 2022.
- [13] Z. Guo, J. Chen, T. He, W. Wang, H. Abbas, and Z. Lv, "Ds-cnn: Dual-stream convolutional neural networks-based heart sound classification for wearable devices," *IEEE Transactions on Consumer Electronics*, vol. 69, no. 4, pp. 1186–1194, 2023.
- [14] A. Tang and W. Zhao, "A fault diagnosis method for drilling pump fluid ends based on time–frequency transforms," *Processes*, vol. 11, no. 7, p. 1996, 2023.
- [15] Z. Chen, S. Tian, X. Shi, and H. Lu, "Multiscale shared learning for fault diagnosis of rotating machinery in transportation infrastructures," *IEEE Transactions on Industrial Informatics*, vol. 19, no. 1, pp. 447–458, 2022.
- [16] B. Song, C. Zheng, Y. Jin, H. Shi, Y. Tao, and S. Tan, "A fault-targeted gated recurrent unit-canonical correlation analysis method for incipient fault detection," *IEEE Transactions on Industrial Informatics*, vol. 20, no. 6, pp. 8739–8748, 2024.
- [17] K.-L. Yin, H.-R. Zhao, Y.-F. Pu, and L. Lu, "Nonlinear active noise control with tap-decomposed robust volterra filter," *Mechanical Systems and Signal Processing*, vol. 206, p. 110887, 2024.
- [18] Y. Zhu, H. Zhao, X. He, Z. Shu, and B. Chen, "Cascaded random fourier filter for robust nonlinear active noise control," *IEEE/ACM Transactions on Audio, Speech, and Language Processing*, vol. 30, pp. 2188–2200, 2021.
- [19] R. Zheng, L. Lin, and H. Yan, "A noise suppression filter for molecular communication via diffusion," *IEEE Wireless Communications Letters*, vol. 10, no. 3, pp. 589–593, 2020.
- [20] M. R. Lone and E. Khan, "A good neighbor is a great blessing: Nearest neighbor filtering method to remove impulse noise," *Journal of King Saud University-Computer and Information Sciences*, vol. 34, no. 10, pp. 9942–9952, 2022.
- [21] X. Wang, J. Chen, X. Chen, J. Guo, and Q. Xiang, "Multichannel iterative noise reduction filters in the short-time-fourier-transform domain based on kronecker product decomposition," *IEEE/ACM Transactions on Audio, Speech, and Language Processing*, vol. 29, pp. 2725–2740, 2021.
- [22] G. Brahmhi, M. Berguig, and L. Harrouchi, "Attenuation of random noise using advanced adaptive filters in post-stack seismic imaging," *Bollettino Di Geofisica Teorica, Ed., Applicata*, vol. 62, no. 3, pp. 387–402, 2021.
- [23] S. Qiao, Y. Fan, G. Wang, D. Mu, and Z. He, "Modified strong tracking slide window variational adaptive kalman filter with unknown noise statistics," *IEEE Transactions on Industrial Informatics*, vol. 19, no. 8, pp. 8679–8690, 2022.
- [24] Z. Liu, M. Zhang, X. Song, and X. Yan, "A novel fusion maximum correntropy kalman/ufir filter for state estimation with uncertain non-gaussian noise statistics," *Measurement*, vol. 220, p. 113339, 2023.
- [25] J. Lee and H. Vandierendonck, "Towards lower precision adaptive filters: facts from backward error analysis of rls," *IEEE Transactions on Signal Processing*, vol. 69, pp. 3446–3458, 2021.
- [26] S. Zhang, Z. Liu, Y. Chen, Y. Jin, and G. Bai, "Selective kernel convolution deep residual network based on channel-spatial attention mechanism and feature fusion for mechanical fault diagnosis," *ISA transactions*, vol. 133, pp. 369–383, 2023.
- [27] Z. Yu, C. Zhang, and C. Deng, "An improved gnn using dynamic graph embedding mechanism: a novel end-to-end framework for rolling bearing fault diagnosis under variable working conditions," *Mechanical Systems and Signal Processing*, vol. 200, p. 110534, 2023.
- [28] K. Yan, C. Lu, X. Ma, Z. Ji, and J. Huang, "Intelligent fault diagnosis for air handling units based on improved generative adversarial network and deep reinforcement learning," *Expert Systems with Applications*, vol. 240, p. 122545, 2024.
- [29] Y. Xue, C. Wen, Z. Wang, W. Liu, and G. Chen, "A novel framework for motor bearing fault diagnosis based on multi-transformation domain and multi-source data," *Knowledge-Based Systems*, vol. 283, p. 111205, 2024.
- [30] K. Zhao, J. Xiao, C. Li, Z. Xu, and M. Yue, "Fault diagnosis of rolling bearing using cnn and pca fractal based feature extraction," *Measurement*, vol. 223, p. 113754, 2023.
- [31] Q. Ni, Z. Zhan, X. Li, Z. Zhao, and L. L. Lai, "A real-time fault diagnosis method for grid-side overcurrent in train traction system using signal time series feature pattern recognition," *IEEE Transactions on Industrial Electronics*, vol. 71, no. 4, pp. 4210–4218, 2023.
- [32] L.-N. Mi, Y.-F. Guo, M. Zhang, and X.-J. Zhuo, "Stochastic resonance in gene transcriptional regulatory system driven by gaussian noise and lévy noise," *Chaos, Solitons & Fractals*, vol. 167, p. 113096, 2023.
- [33] C. Meng, J. Gao, Y. Tian, L. Zhao, H. Zhao, and Z. Wang, "Attenuation of seismic random noise with unknown distribution: A gaussianization framework," *IEEE Transactions on Geoscience and Remote Sensing*, vol. 61, pp. 1–15, 2023.
- [34] R. Yan, Z. Shang, H. Xu, J. Wen, Z. Zhao, X. Chen, and R. X. Gao, "Wavelet transform for rotary machine fault diagnosis: 10 years revisited," *Mechanical Systems and Signal Processing*, vol. 200, p. 110545, 2023.
- [35] Z. Zhang, D. Guo, S. Zhou, J. Zhang, and Y. Lin, "Flight trajectory prediction enabled by time-frequency wavelet transform," *Nature Communications*, vol. 14, no. 1, p. 5258, 2023.
- [36] C. Chen, H. Lu, H. Hong, H. Wang, and S. Wan, "Deep self-supervised graph attention convolution autoencoder for networks clustering," *IEEE Transactions on Consumer Electronics*, vol. 69, no. 4, pp. 974–983, 2023.
- [37] S. Yan, H. Shao, Y. Xiao, B. Liu, and J. Wan, "Hybrid robust convolutional autoencoder for unsupervised anomaly detection of machine tools under noises," *Robotics and Computer-Integrated Manufacturing*, vol. 79, p. 102441, 2023.
- [38] D. Zhang, B. Chen, H. Zhu, H. H. Goh, Y. Dong, and T. Wu, "Short-term wind power prediction based on two-layer decomposition and bitcnn-bilstm-attention model," *Energy*, vol. 285, p. 128762, 2023.
- [39] Z. Liu, Y. Wang, S. Vaidya, F. Ruehle, J. Halverson, M. Soljačić, T. Y. Hou, and M. Tegmark, "Kan: Kolmogorov-arnold networks," *arXiv preprint arXiv:2404.19756*, 2024.
- [40] E. Jakobsson, E. Frisk, M. Krysander, and R. Pettersson, "A dataset for fault classification in rock drills, a fast oscillating hydraulic system," in *Annual Conference of the PHM Society*, vol. 14, no. 1, 2022.
- [41] D. Ruan, J. Wang, J. Yan, and C. Gühmann, "Cnn parameter design based on fault signal analysis and its application in bearing fault diagnosis," *Advanced Engineering Informatics*, vol. 55, p. 101877, 2023.
- [42] F. Dao, Y. Zeng, and J. Qian, "Fault diagnosis of hydro-turbine via the incorporation of bayesian algorithm optimized cnn-lstm neural network," *Energy*, vol. 290, p. 130326, 2024.
- [43] A. Mohammad-Alikhani, B. Nahid-Mobarakeh, and M.-F. Hsieh, "One-dimensional lstm-regulated deep residual network for data-driven fault detection in electric machines," *IEEE Transactions on Industrial Electronics*, vol. 71, no. 3, pp. 3083–3092, 2024.